# Anisotropic Metasurfaces as Tunable SERS Substrates for 2D Materials

Vrinda Thareja,[†] Majid Esfandyarpour,[†] Pieter G. Kik,[†,‡] and Mark L. Brongersma*[,†]

[†]Geballe Laboratory for Advanced Materials, Stanford University, Stanford, California 94305, United States
[‡]CREOL, The College of Optics and Photonics, University of Central Florida, 4000 Central Florida Boulevard, Orlando, Florida 32816, United States

ABSTRACT: The reflection of light from metallic mirrors results in a near-zero electric field at their surface. This precludes strong light−matter interaction between such mirrors and two-dimensional (2D) materials placed in direct contact with them. Patterning of the metal surfaces with subwavelength grooves can produce anisotropic metasurfaces that offer robust enhancements in the magnitude and control over the direction of the surface fields. Here, we use this control to analyze the Raman tensor for vibrational modes of atomically thin graphene. The anisotropic nature of the grooves leads to different Raman signal enhancement for the G (25 times) and 2D (50 times) Raman peaks of graphene for optimized groove dimensions. A notable suppression of these peaks by 40% for specific groove dimensions is also achieved. These findings suggest the use of metasurfaces as tunable surface-enhanced Raman scattering substrates to study the vibrational modes of 2D materials with reduced background signals.

KEYWORDS: anisotropic metasurfaces, SERS, plasmonics, graphene, Raman tensor, 2D materials
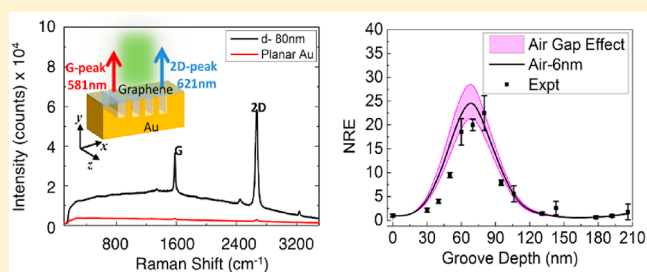
The optical properties of metallic nanostructures have enjoyed great interest from the scientific community for many years.[1] When light is incident on a metallic nanostructure, it drives collective oscillations of electrons, referred to as a localized surface plasmon resonance (LSPR).[2] Plasmon excitations can be used to concentrate light near the metal surface. The resulting increase in the electric fields explains the enhanced Raman signals recorded in 1977 from pyridine molecules on a roughened silver electrode and has since led to many practical applications in the field of surface-enhanced Raman scattering (SERS).[3−8] The development of plasmonics-based SERS substrates and the nanoscale control of electromagnetic fields recently received renewed attention with the prospect of making high-performance biosensors as well as sensitive detectors for chemical warfare agents, surface contaminants, and even single molecules.[9−13]

Conventional SERS experiments typically rely on substrates made from roughened gold and silver films, colloidal aggregates, or coatings of nanoparticles to generate large field enhancements.[9,13] Unfortunately, the exact signal enhancements so generated are generally unpredictable, unstable, and nonreproducible due to the high sensitivity of the Raman signal to the surface topography. Moreover, Raman substrates typically also do not offer control over the local direction of the electric fields in their vicinity. Such control would greatly increase the power of arranging and analyzing molecules of interest.[6−8,14] For example, to learn about the local structure, symmetry of the bond vibrations, and orientation of molecules and crystals, it would be highly desirable to develop SERS substrates capable of controllably enhancing and locally orienting fields.

Electric mirrors based on smooth and highly conductive metal films provide reduced electric field strengths at their surfaces due to the phase reversal of light upon reflection. When such a mirror is illuminated at normal incidence, the first maximum in the electric field is observed at a quarter-wavelength distance above its surface. This is why thin absorber layers are typically spaced this distance from the metal surfaces, in the so-called Salisbury screen configuration first developed in the radar field and more recently used in the IR to boost absorption within graphene.[15,16]

Patterning the surface of a metal film with subwavelength holes or grooves results in the creation of a metasurface with a modified reflection phase.[17] Such metasurfaces were recently used to increase the performance of thin organic solar cells.[18] Here, we will employ an anisotropic metasurface composed of a dense array of parallel grooves patterned into a metal surface. The optical properties of such metasurfaces are governed by the excitation of propagating gap plasmons in the grooves as opposed to localized particle resonances. For this reason, the generated fields are less sensitive to the local topography and can provide more robust and engineerable field enhancements in controlled orientations. This opens the possibility to study the unique vibrational properties of 2D materials, which have recently attracted significant attention, as they control many
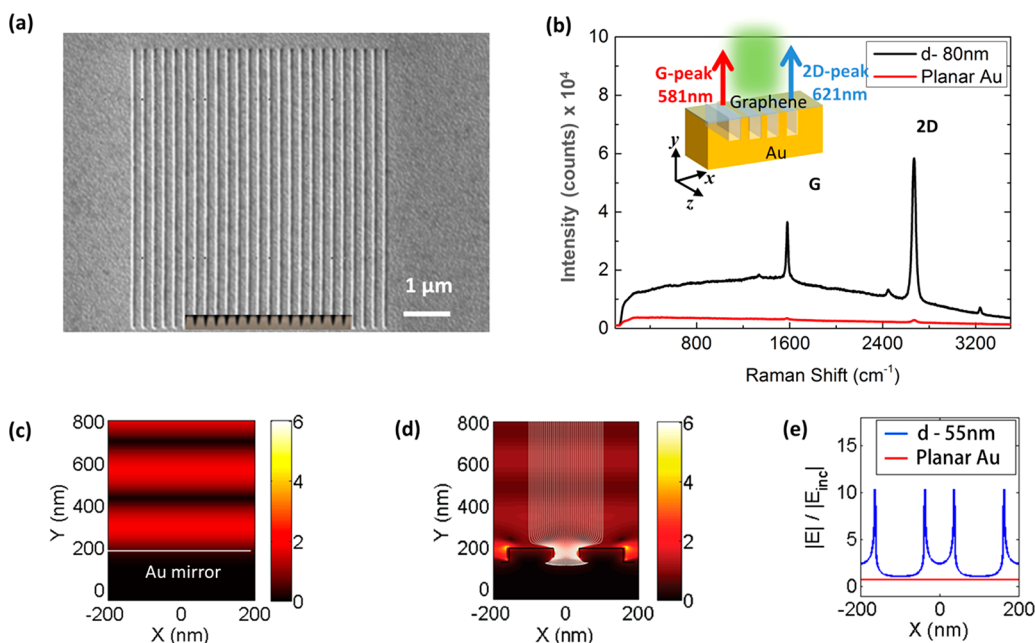
Figure 1. Enhancing Raman signals with anisotropic metasurfaces. (a) SEM image of the fabricated metasurface with a cross-sectional SEM of the gratings under the SEM image. (b) Raman spectrum of monolayer graphene placed on a smooth, optically thick Au film (red curve) and a Au metasurface created by focused ion beam milling of an array with 75 nm wide and 80 nm deep grooves (black curve). Inset: Sample schematic. (c) Map of the electric field magnitude for a normally incident light wave at 532 nm reflecting from a planar gold film. (d) Map of the electric field magnitude for a normally incident light wave at 532 nm reflecting off a metasurface with 75 nm wide and 55 nm deep grooves spaced at a 200 nm period. (e) Line cut (blue) showing the variation of the electric field amplitude at the metasurface shown in panel d. Also shown is the electric field amplitude line cut (red) for an unpatterned Au surface for comparison. The field magnitudes are normalized to the incident electric field amplitude.

electronic, optical, and thermal properties.[19,20] Here, we illustrate this idea with the topical material graphene.[21−24] Given its two-dimensional nature and distinct vibrational properties, graphene represents an ideal test case to evaluate the effect of anisotropic field enhancement on Raman scattering across a large area metasurface.[25−34] In this work, we demonstrate a systematic tuning of the Raman signal of graphene upon changing the underlying dimensions of the metasurfaces. With the anisotropic nature of metasurfaces composed of linear groove arrays, the Raman signals reflect the properties of the Raman polarizability tensor, which is distinct for different phonons in graphene.

To determine the benefits of using a metasurface in Raman experiments on 2D materials, we pattern a variety of subwavelength groove arrays into a gold (Au) surface by focused ion beam milling. Figure 1(a) shows top-view and cross-sectional scanning electron microscope (SEM) images of a fabricated metasurface in Au with a periodicity $P = 200$ nm, a width $w = 75$ nm, and a depth $d = 80$ nm. As a Raman probe material, we place single-layer, CVD-grown graphene directly on the metasurfaces by layer transfer and analyze its Raman signals in a confocal microscope connected to a spectrometer (see Methods). Figure 1(b) shows the Raman spectrum of graphene when placed on an as-deposited Au film (red curve) and on the metasurface shown in Figure 1(a) (black curve). The inset to Figure 1(b) schematically illustrates the experimental geometry. For a normally incident pump at a wavelength of 532 nm, the Raman spectrum of the graphene-coated unpatterned Au surface shows two weak Raman peaks at 581 and 621 nm, namely, the G-peak and 2D-peak, respectively, superimposed on a broad Au luminescence background.[35−37] The G and 2D Raman peaks are the dominant peaks in the Raman spectrum for pristine graphene

and are commonly used to indicate the presence of graphene. The D-peak, on the other hand, is associated with the existence of defects within graphene and depending on the quality of graphene may or may not be present. These peaks are significantly enhanced for the graphene-coated metasurface. The optimization and physical origin of the observed enhancements are discussed in detail in this paper. We will start with a discussion of the electromagnetic properties of the proposed metasurfaces.

Both the excitation and collection of Raman signal can be enhanced using a patterned metasurface. We will start by showing how the excitation of the Raman signal can be enhanced by choosing the correct groove dimensions when using a certain pump laser. Figure 1(c) and (d) show electromagnetic simulations for a 532 nm wavelength pump wave that is normally incident on either a smooth Au surface or a metasurface composed of an array of 55 nm deep and 75 nm wide grooves. The field magnitude above the smooth Au film shows a standing wave pattern with a minimum close to the surface and several maxima at different heights above the surface where the field magnitude reaches about twice the incident field strength. The near-surface field minimum results from the approximately π phase reversal for the electric field upon reflection, as would be expected for a normal (electric) mirror. Figure 1(d) shows the field distribution above the metasurface with the incident field polarized normal to the length of the grooves. The metasurface also generates a standing wave pattern, but in this case the field maxima are displaced to produce a field maximum right at the metasurface (connecting the tops of the grating teeth). The field strength at the surface also reaches significantly larger values than those observed above the flat gold film.
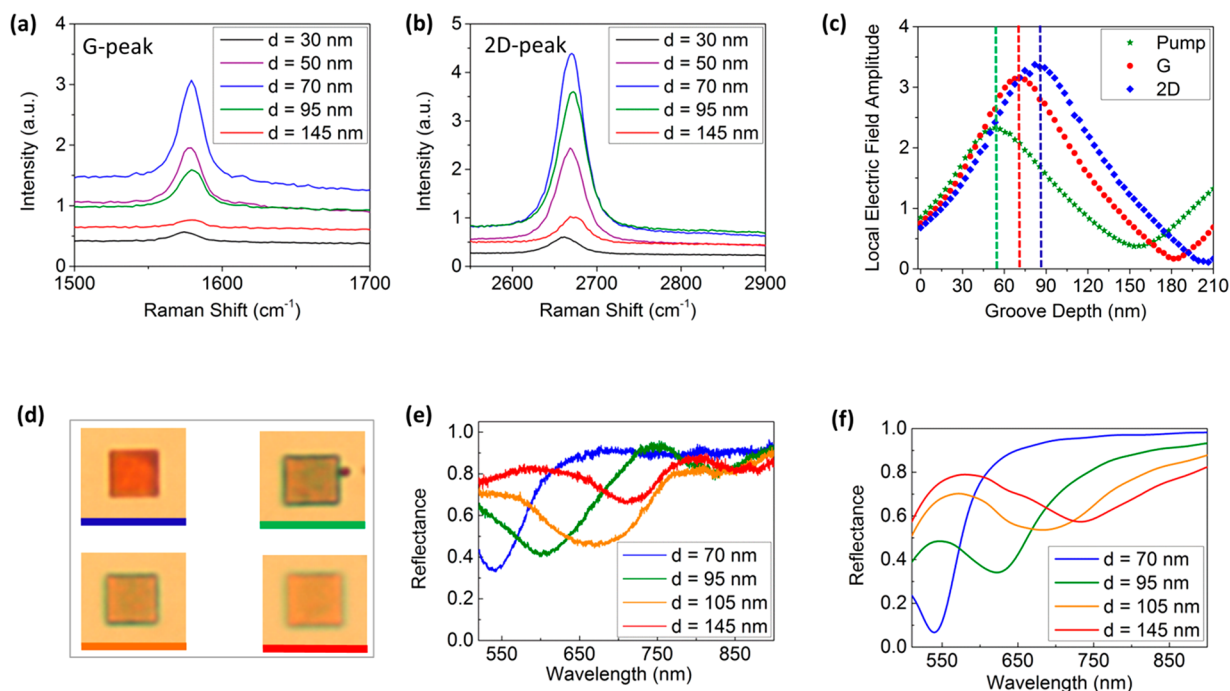
Figure 2. Variation of the Raman signal and reflectance from the graphene-coated metasurface with groove depth. Zoomed-in Raman spectra showing (a) the G-peak and (b) the 2D-peak of graphene and their variation in strength for different groove depths d. (c) Local electric field amplitude within graphene (for three different wavelengths corresponding to pump, G-peak, and 2D-peak) as a function of groove depth for 75 nm wide gratings. (d) Optical images of graphene-coated metasurfaces for different groove depths. The colored strip at the base of the images corresponds to the groove depth color code in the next figure: e. (e) Experimentally measured reflection spectra as a function of groove depths. (f) Theoretically predicted reflectance spectra for the same groove depths as shown in e.

The near-surface field enhancement on the metasurface is attributed to a combination of effects. First, the grooves support propagating surface plasmon polaritons (SPPs) known as gap plasmons that can be excited by the incident plane wave. These SPPs reflect from the bottom of the groove, and the interference of the incident and reflected SPP fields gives rise to local field enhancements and suppressions. Without dissipative losses, such interference can give rise to a doubling in the electric field strength at the surface when the groove depth is approximately $\lambda_{inc}/4n_{SPP}$, where n_{SPP} is the gap plasmon mode index. For a metasurface with this groove depth, the maximum in the electric field at the surface is accompanied by a minimum in the magnetic field. For this reason, these metasurfaces are also sometimes called magnetic mirrors.[17] We denote this electric field enhancement due to interference as seen for a Salisbury screen as η_S. Second, the coupling of the incident plane wave to the gap plasmons in the grooves is facilitated by the process of magnetoelectric interference that is seen for resonant optical antennas.[38] It leads to a funneling of energy into the grooves from a cross-sectional area that is larger than the geometrical area of the grooves. This can be visualized by the extinction Poynting vector that is superposed onto the field plot in Figure 1(d). The lateral concentration of light within the grooves leads to another enhancement in the electric field denoted as η_{LC}. For an optimized case in which all of the incident light would flow into the grooves, the magnitude of η_{LC} will approximately be equal to the ratio of the groove period and the width P/w.[39] This follows from the continuity of the (average) tangential electric field at the metasurface and the effective screening of the electric field inside the high-conductivity metal teeth. Third, the sharp edges of the groove further enhance the

electric field by charge accumulation in these areas (i.e., the lightning rod effect). This effect is clearly seen in Figure 1(e), which shows a line cut of the electric field amplitude normalized to the incident electric field amplitude along the metasurface. The spikes in the electric field amplitude associated with the sharp groove edges are very sensitive to the exact groove edge shape and less controlled than the enhancements resulting from SPP reflection and energy funneling. This publication is primarily focused on manipulating the first two effects, which are easier to accurately control in the groove fabrication. For comparison, the electric field amplitude distribution for a planar Au surface is also shown in Figure 1(e). The enhancements in the electric field at the grooved metal surface resulting from SPP reflection η_S and lateral concentration η_{LC} are independent and thus cascade to produce a total enhancement $\eta_T = \eta_S \times \eta_{LC}$. Based on the arguments above, we could expect to see controllable field enhancements (away from sharp corners) of ∼5.3 times for the considered subwavelength groove array with a periodicity $P = 200$ nm and a groove width $w = 75$ nm. Such field enhancements can give rise to notable and reproducible enhancements in experimental Raman signals. These fields are also oriented orthogonal to the groove direction, characteristic for the fields of the gap plasmons. At this point, it is worth noting that different metasurface designs can reshape surface fields differently in terms of the magnitude and direction of the local electric field enhancement. The differences in the vector fields at the metasurface manifest themselves as different Raman signal enhancements for the various metasurface dimensions. This is the topic of the next sections.

Theoretically, the Raman signal enhancement factor, EF, for a material with an isotropic Raman polarizability is linked to

the local electric field (E_{Loc}) at the location of the Raman-active material at the pump frequency (ω_L) and the Raman scattered frequency (ω_R) as

$$EF = |\tilde{E}_{Loc}(\omega_L)|^2 |\tilde{E}_{Loc}(\omega_R)|^2 \qquad (1)$$

where $\tilde{E}_{Loc}$ is the local electric field at the respective frequency normalized to the incident electric field at that frequency.[40] When the Raman shift is small ($\omega_L \approx \omega_R$), a dependence of EF on the fourth power of the electric field enhancement, $\tilde{E}_{Loc}$, is expected. For this reason, Raman signals provide a sensitive probe for local field enhancements.

We experimentally investigate the effect of the metasurface geometry on the Raman enhancement factor by fabricating three sets of groove arrays with groove widths of 75, 95, and 170 nm, respectively, all having a fixed periodicity of 200 nm. For each set, the groove depth was varied in 13 steps from 30 to 210 nm, resulting in a total of 39 groove arrays, each with an area of 5×5 μm^2. Figure 2(a) and (b) display Raman spectra obtained from five separate graphene-covered groove arrays, each with the same groove width of 75 nm, showing the evolution of the G-peak (581 nm) and the 2D-peak (621 nm), respectively, as a function of groove depth. Both peaks initially increase in strength as the groove depth is increased from 30 nm to 70 nm and reduce in strength for larger groove depths. Notably, the G-peak drops more quickly than the 2D-peak as a depth of 95 nm is reached, showing that both peaks have a significantly different dependence on groove depth.

To qualitatively understand the above dependence of the Raman signal on groove depth, we first simulate the electric field at the center of the groove entrance as a function of groove depth for 75 nm wide grooves using electromagnetic simulations based on the finite-different time-domain (FDTD) technique. The metasurfaces are modeled as a periodic array of air-filled grooves patterned into a semi-infinite Au layer. A sheet of graphene is then placed on the metasurface and modeled as a layer with an effective thickness of 0.5 nm and a conductivity given by the Kubo formalism.[41] Using the Drude model, it is possible to assign an effective dielectric constant to graphene.[42−44] A plane-wave source is used to direct a light wave polarized perpendicular to the groove length toward the groove array at normal incidence. Periodic boundary conditions are applied on the left- and right-hand sides of a groove to generate the metasurface. On the top and bottom edges, a perfectly matched layer (PML) is placed. In the cross-sectional SEM images of our gratings we had observed rounded groove edges (Figure 1(b)). We have taken this into consideration in our theoretical model by rounding off the corners of our rectangular grooves with a 30 nm radius of curvature. In comparing the simulated and experimentally observed Raman signal strengths, we obtained the best quantitative agreement when we assume the presence of an air gap of 6 nm between the graphene layer and the underlying metasurface. The introduction of this spacer slightly lowers the simulated field magnitude and Raman signal for all metasurfaces. Physically, it may account for the presence of a small spacing between the graphene layer and metasurfaces due to surface contamination or an inaccurate capture of the exact shape/curvature of the groove corners. Later we will show how the dependence of this ad hoc assumption of an air gap impacts the simulation results and demonstrate that the results are qualitatively similar for different air gaps.

Figure 2(c) shows the simulated field enhancement as a function of groove depth at the pump wavelength (green

curve), G-peak wavelength (red curve), and 2D-peak wavelength (blue curve) for a metasurface with 75 nm wide grooves. The largest field for the pump wavelength is observed at a groove depth of approximately 55 nm. Based on a simple standing wave argument for perfectly rectangular grooves one would expect the optimal groove depth for maximizing the field at the location of graphene to be at a quarter SPP wavelength above the bottom of the groove: $d \approx \lambda_0/4n_{SPP}$, as argued above. For a calculated value for n_{SPP} of 1.5 for 75 nm wide grooves, the optimum groove depth would be 88 nm. This mismatch is attributed to a notable reflection phase at the entrance of the groove.[45] Given that the Raman enhancement is a product of the excitation (pump) field enhancement and collection field enhancement (eq 1), we expect the highest Raman signal for a given Raman line to occur for a groove depth that provides large field enhancement at both the excitation and collection wavelengths. For the G-peak, we would thus expect that the maximum Raman enhancement will occur at a groove depth in the range from 55 and 70 nm (between the red and green dashed lines in Figure 2(c)), while for the 2D peak it will occur for groove depths in the range from 55 and 80 nm (between the green and blue dashed lines in Figure 2(c)).

To directly demonstrate the wavelength tunability of the grooved metasurfaces, we record spatially resolved reflection spectra of the graphene-coated metasurfaces using a Nikon confocal spectrometer. A 20× low-NA objective was chosen for the measurements to ensure near-normal incidence illumination and collection. Figure 2(e) shows the reflectance spectra measured from four different metasurfaces having a fixed groove width of 75 nm and measured groove depths averaging 70, 95, 105, and 145 nm as obtained from scanning electron microscopy images. The accuracy of the focused ion beam (FIB) milling results in depth variation from groove to groove of about 5 nm. Figure 2(d) shows bright field optical microscopy images of these metasurfaces. They display reasonably uniform colors across the surface. Horizontal stripes at the bottom of each optical image are color-coded to match the color convention of the reflectance curves for the different groove depths in Figure 2(e). We observe that the reflectance minimum shifts to a longer wavelength with increasing groove depth, consistent with the resonance condition for the grooves ($d \approx \lambda_0/4n_{SPP}$). We use the FDTD model described before to theoretically predict the reflectance curves, and these are shown in Figure 2(f). The theoretically estimated spectral locations of the reflectance minima match well with the experimentally observed reflectance spectra. As with the experiments, we notice a red-shift of the reflectance dip upon increasing the groove depth for our theoretical predictions.

The tunability of the groove resonances indicates the opportunity to realize tunable electric field enhancements at the groove opening, exactly where the graphene is located. We measure the resulting Raman signal enhancements at 25 different points for each of the 39 graphene-coated groove arrays (see Methods) and find an averaged Raman signal for each grating. We then subtract the broad background arising due to Au fluorescence from the area under the concerned Raman peaks. We obtain the Raman signal enhancement for different metasurfaces by integrating the counts under the relevant background-subtracted Raman peaks from a patterned area and normalize them to the counts obtained under the respective peaks on a smooth metal region. The Raman

enhancement so obtained is termed the normalized Raman enhancement (NRE). The dependence of the NRE on groove depth for the G-peak is plotted in Figure 3 for different groove
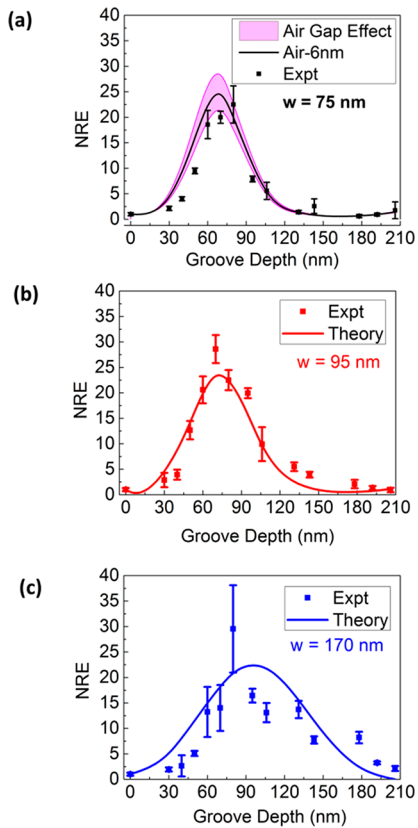
Figure 3. Normalized G-peak Raman enhancement dependence on groove depth and width. Normalized Raman enhancement (NRE) vs groove depth for the G-peak, corresponding to grating groove widths of (a) 75 nm (black), (b) 95 nm (red), and (c) 170 nm (blue). The dots indicate the experimental observations, and the solid curves indicate the theoretical predictions based on FDTD and assuming an air gap of 6 nm between the metal and graphene layer. The pink band in (a) shows the sensitivity of the NRE to the choice of air gap with the lower end of the band corresponding to an air gap of 7 nm and the top of the band corresponding to an air gap of 5 nm.

widths. The error bars associated with each dot represent the standard deviation from the mean enhancement for the 25 measurements collected on each grating. Figure 3(a) shows that for the groove width of 75 nm the Raman signal exhibits a maximum at a groove depth of about 70 nm. As expected from the discussion above, this optimum groove depth lies between those depths where the maximum field enhancements of the pump and the Raman scattered light are achieved (see Figure 2(c)). Figure 3(b) and (c) show the corresponding results for arrays with wider grooves, and these exhibit the maximum NRE at larger groove depths. These observations are consistent with a reduced gap SPP mode index for wider grooves,[2] requiring the use of deeper grooves to reach the $d = \lambda_0/4n_{SPP}$ condition. A similar shift is also observed for the adjacent minimum at larger groove depths, where about half a gap plasmon wavelength fits along the depth of the grooves. As expected, for the 75 nm wide grooves, this minimum occurs about $d = \lambda_0/4n_{SPP} \approx 90$ nm to the right of the groove depth responsible for maximum NRE (see Figure 3a). Interestingly,

there are a few groove depths for which the measured NRE $\lesssim$ 1, indicating a controlled Raman signal suppression.

Next, we aim to quantitatively model the dependence of the NRE from graphene on the groove dimensions. To this end, we will assume our experimental configuration in which the sample is illuminated with normally incident light that is polarized perpendicular to the grooves (to maximize the excitation enhancement). The detection of the Raman-shifted emission is collected at normal exit to the surface and without a polarization filter to allow collection of Raman signals polarized along (z-direction) and perpendicular (x-direction) to the grooves. The Raman enhancement expression as shown in eq 1 is for materials with an isotropic Raman polarizability. Graphene does not fall in that category and has an anisotropic Raman polarizability instead. When light at a frequency ω_L is incident on a graphene surface, the local field vector $\overline{E}_{Loc}(\omega_L)$ induces a Raman dipole moment $\overline{p}$ at shifted frequency ω_R:

$$\overline{p}(\omega_R) = \hat{\alpha} \cdot \overline{E}_{Loc}(\omega_L) \tag{2}$$

where $\hat{\alpha}$ is the Raman polarizability tensor.[40]

The enhancement in the local excitation field in the presence of the metasurface is given by $\tilde{E}_{Loc}(\omega_L)$, defined as the ratio of the local field $\overline{E}_{Loc}(\omega_L)$ to the incident field. The collection efficiency in the detector can also be enhanced by the metasurface. Its magnitude can be assessed by invoking optical reciprocity.[40] Based on this theorem, the collection enhancement of the Raman signal with a given polarization is linked to the local field enhancement $\tilde{E}_{Loc}(\omega_R)$ in the graphene as generated by a plane-wave excitation at the Raman-shifted frequency launched backward from the detector with this same polarization. The total Raman signal enhancement factor for polarized detection then becomes

$$EF = |\tilde{E}_{Loc}(\omega_R) \cdot \hat{\alpha}_N \cdot \tilde{E}_{Loc}(\omega_L)|^2 \tag{3}$$

where $\hat{\alpha}_N$ is the normalized polarizability tensor characterizing the symmetry of $\hat{\alpha}$. Depending on the Raman scattering properties of the material (i.e., $\hat{\alpha}_N$) or substrate (i.e., an anisotropic groove array), the EF need not be the same for both detection polarization directions. For the case of unpolarized detection, the enhancement factor is simply the sum of the enhancement factors corresponding to detection polarization directions parallel (labeled $\parallel$) or perpendicular (labeled $\perp$) to the groove direction:

$$EF = |\tilde{E}_{Loc,\parallel}(\omega_R) \cdot \hat{\alpha}_N \cdot \tilde{E}_{Loc}(\omega_L)|^2$$
$$+ |\tilde{E}_{Loc,\perp}(\omega_R) \cdot \hat{\alpha}_N \cdot \tilde{E}_{Loc}(\omega_L)|^2 \tag{4}$$

It is well known that the intensities of the G- and the 2D-peaks and hence the EF on planar surfaces are independent of the orientation of graphene with respect to the incident light.[46] To obtain the Raman enhancement factor for graphene-covered metasurfaces, it is important to understand the Raman scattering properties embodied in the polarizability tensor of graphene for the concerned vibrational modes.

The Raman spectrum of graphene shows two important peaks in the considered spectral range, namely, the G-peak and the 2D-peak. The G-peak arises from a conventional first-order Raman scattering process in graphene. It is associated with doubly degenerate in-plane transverse optical (iTO) and longitudinal optical (LO) phonon modes that exhibit E_{2g} symmetry at the Brillouin zone center. The 2D-peak, on the other hand, originates from a second-order scattering process

involving two iTO phonons near the K point that correspond to A_{1g} symmetry. Let us first focus our attention on the 2D-peak. Since the scattering for this band is due to in-plane phonons, the polarizability tensor for the 2D-band is isotropic in the plane of graphene and zero out of plane. If the graphene sheet lies in the $x-z$ plane, the form of the polarizability tensor for the 2D-band is given by[46,47]

$$\hat{\alpha}_N = \begin{pmatrix} 1 & 0 & 0 \\ 0 & 0 & 0 \\ 0 & 0 & 1 \end{pmatrix} \tag{5}$$

Using eq 4 to calculate local enhancements of the Raman signal on the metasurface, we spatially average the Raman enhancement factors in the graphene layer across the metasurface:

$$\text{EF}|_{\text{2D-peak}}$$
$$= \langle |\tilde{E}_{\text{Loc},\parallel}(\omega_{2D}) \cdot \hat{\alpha}_N \cdot \tilde{E}_{\text{Loc}}(\omega_L)| + |\tilde{E}_{\text{Loc},\perp}(\omega_{2D}) \cdot \hat{\alpha}_N \cdot \tilde{E}_{\text{Loc}}(\omega_L)| \rangle \tag{6}$$

where the brackets represent spatial averaging and $\parallel$ and $\perp$ refer to the parallel and perpendicular detection polarizations with respect to the length of the grooves. Note that the first term in this expression will be zero based on our experimental setup, as the Raman dipole for the 2D peak will be excited normal to the groove length.

The Raman polarizability tensors of the G-peak are doubly degenerate for the E_{2g} symmetry and assume the following form:[46,47]

$$E_{2g}(1) = \hat{\alpha}_{N,1} = \begin{pmatrix} 1 & 0 & 0 \\ 0 & 0 & 0 \\ 0 & 0 & -1 \end{pmatrix}$$

$$E_{2g}(2) = \hat{\alpha}_{N,2} = \begin{pmatrix} 0 & 0 & 1 \\ 0 & 0 & 0 \\ 1 & 0 & 0 \end{pmatrix} \tag{7}$$

For the G-peak, averaging eq 4 across the graphene layer yields

$$\text{EF}|_{\text{G-peak}} = \frac{1}{2} \langle |\tilde{E}_{\text{Loc},\parallel}(\omega_G) \cdot \hat{\alpha}_{N,1} \cdot \tilde{E}_{\text{Loc}}(\omega_L)|^2$$
$$+ |\tilde{E}_{\text{Loc},\parallel}(\omega_G) \cdot \hat{\alpha}_{N,2} \cdot \tilde{E}_{\text{Loc}}(\omega_L)|^2$$
$$+ |\tilde{E}_{\text{Loc},\perp}(\omega_G) \cdot \hat{\alpha}_{N,1} \cdot \tilde{E}_{\text{Loc}}(\omega_L)|^2$$
$$+ |\tilde{E}_{\text{Loc},\perp}(\omega_G) \cdot \hat{\alpha}_{N,2} \cdot \tilde{E}_{\text{Loc}}(\omega_L)|^2 \rangle \tag{8}$$

With the knowledge of the polarizability tensors and our chosen laser polarization normal to the grooves, we find that the enhancement factors for the 2D- and the G-peaks of graphene depend only on the scalar product of the x and z components of the local electric field enhancement factors, written as $\tilde{E}_x$ and $\tilde{E}_z$. This reduces the spatially averaged Raman enhancement factors to the following form:

$$\text{EF}|_{\text{2D-peak}} = \langle |\tilde{E}_{x,\perp}(\omega_{2D}) \, \tilde{E}_{x,\perp}(\omega_L)|^2 \rangle \tag{9}$$

$$\text{EF}|_{\text{G-peak}} = \frac{1}{2} \langle |\tilde{E}_{x,\perp}(\omega_G) \, \tilde{E}_{x,\perp}(\omega_L)|^2$$
$$+ |\tilde{E}_{z,\parallel}(\omega_G) \, \tilde{E}_{x,\perp}(\omega_L)|^2 \rangle \tag{10}$$

We obtain the normalized Raman enhancement factor by dividing the results of eqs 9 and 10 by the corresponding

results on a flat metal substrate. The solid lines in Figure 3(a–c) represent these theoretical predictions of the NRE. The theoretical curves display good quantitative agreement with the experimental observations in terms of the magnitude of the enhancement, the groove depth providing the maximum Raman enhancement, and the width of the enhancement peak vs groove depth. Figure 3(a) also includes simulation results assuming a smaller (5 nm) and larger (7 nm) air gap between graphene and the metasurface, shown as the upper and lower bounds of the shaded region, respectively. Quantitative differences are observed in the overall strength of the Raman signal, but the functional dependence of the Raman signal with groove depth appears quite robust. These observations reflect the sensitivity of the Raman signal to the exact field magnitude, but also indicate the important role groove resonances play in enhancing the Raman signal. This suggests that the measured enhancement factors are not dominated by the presence of local hot spots and inhomogeneous analyte distributions, which is a common challenge in SERS experiments.

The above analysis was carried out to explain the NRE trends for the G-peak of the graphene Raman spectra. We performed a similar analysis for the 2D-peak of graphene, and the observed results are shown in Figure 4. The dots represent the experimentally attained NRE as a function of groove depth for the three different sets of metasurfaces corresponding to
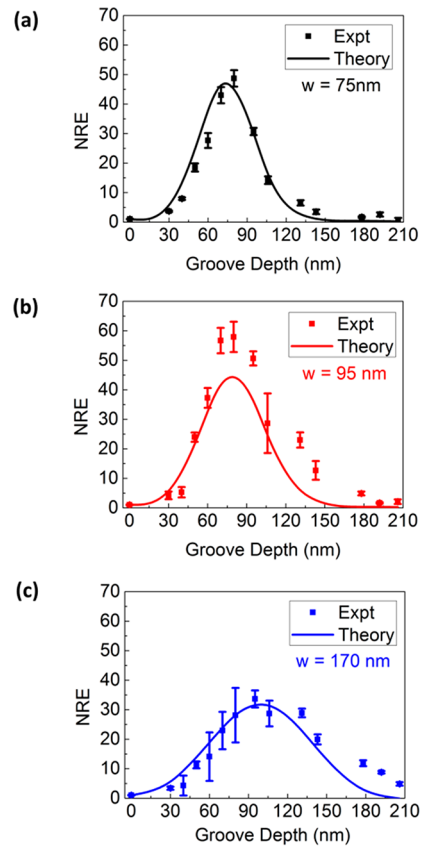
Figure 4. Normalized 2D-peak Raman enhancement dependence on groove depth and width. Normalized Raman enhancement (NRE) vs groove depth for the 2D- peak, corresponding to grating groove width of (a) 75 nm (black), (b) 95 nm (red), and (c) 170 nm (blue). The dots indicate the experimental observations, and the solid lines indicate the theoretical predictions based on FDTD.
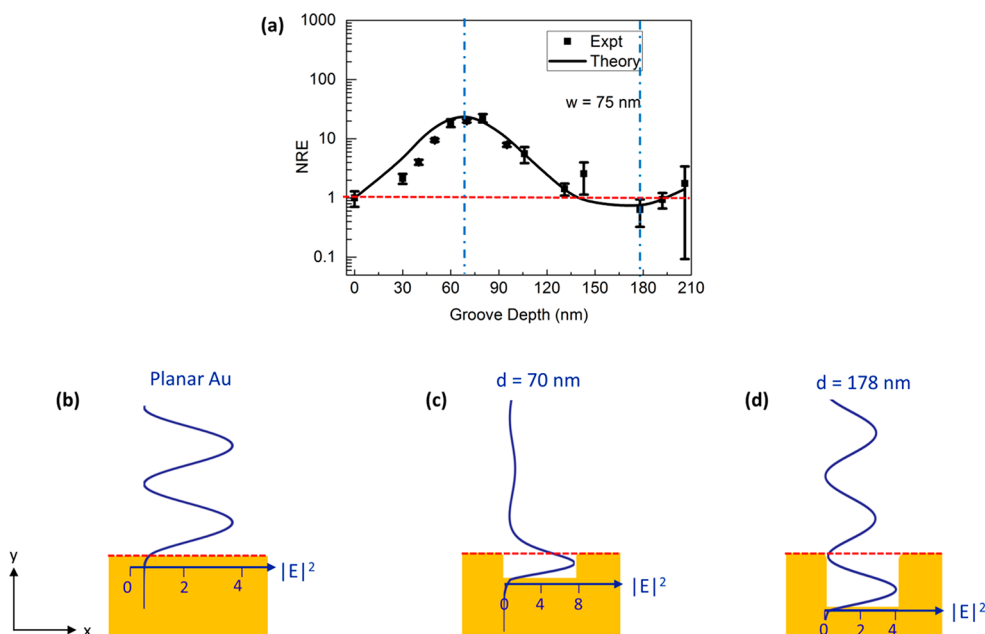
Figure 5. Physical picture for Raman signal enhancement and suppression. (a) Log-scale plot of the experimental (dots) and theoretical (solid line) NRE vs groove depth for the G-peak corresponding to a grating groove width of 75 nm. Absolute squared electric field at the center of the groove entrance at a wavelength of 532 nm for (b) planar Au, (c) a metasurface with a groove depth of 70 nm, and (d) a metasurface with a groove depth of 178 nm.

three different groove widths as before. The experimental analysis of the Raman spectra was carried out in exactly the same way as discussed before for Figure 3. The error bars associated with each dot represent as before the standard deviation from the mean enhancement for the 25 measurements collected corresponding to each groove depth. The solid curves superimposed on the experimental data represent the NRE determined theoretically. The theoretical determination of NRE involves the same structural setup as that used for the generation of Figure 3 except that now the two simulations to calculate the local fields within graphene are performed at the 532 nm pump wavelength and 621 nm Raman-shifted wavelength for the 2D-peak. Again, good agreement is observed between the theoretical predictions and experimental observations.

A noteworthy feature in both the theoretical and experimental data is that the NRE for the 2D-peak is larger than for the G-peak. At the groove depth corresponding to the maximum Raman enhancement, the 2D-peak NRE is approximately 2 times higher than that for the G-peak. This arises due to the different Raman signal collection enhancement for the fundamental phonon modes associated with the G- and the 2D-peaks. With the optical excitation perpendicular to the grooves, the lattice vibrations that give rise to the G-peak produce Raman dipoles both along and perpendicular to the grooves (per eq 7). The collection is only notably enhanced for the Raman dipoles perpendicular to the grooves, as they benefit from coupling to the groove resonances. On the other hand, the radial breathing mode that gives rise to the 2D-peak only produces a Raman dipole along the incident field direction. In our experiment this is the favorable direction perpendicular to the grooves that enjoys a large collection enhancement. As an insignificant collection enhancement is observed for Raman dipoles aligned along the groove, the 2D-peak will experience approximately twice the enhancement seen for the G-peak. From this observation, it is clear that the

tensorial nature of the Raman polarizability can be exposed and quantitatively analyzed with an anisotropic metasurface.

Now we focus our attention on the experimental results and theoretical predictions in Figure 3(a), wherein the NRE $\lesssim$ 1 for a few groove depths. Suppression can be utilized to reduce background signal in sample areas that are not of interest. In order to explore this effect in greater detail and to understand this effect more, we plot the NRE for the G-peak on a logarithmic scale as a function of groove depth for 75 nm wide grooves (see Figure 5(a)). A red dotted line indicating an NRE of 1 is superimposed on the experimental curve to highlight the groove depths for which NRE < 1. We consider two cases; the first one corresponds to a groove depth around 180 nm for which NRE $\approx$ 0.63 < 1. The second case corresponds to a groove depth of 70 nm for which NRE $\approx$ 20. Based on eq 3, the enhancement factor is dependent on the absolute square of the electric fields at the pump wavelength (532 nm) and G-peak wavelength (581 nm) at the location of graphene. These fields provide the Raman excitation and collection enhancements. Figure 5(b−d) illustrate how the fields above the smooth metal surface are changed when grooves of 70 nm (Figure 5c) and 178 nm (Figure 5d) are dug into the surface at the pump wavelength. The Raman-scattered wavelength shift of the G-peak is only 9% with respect to the pump wavelength; as a result, the field distribution relevant for the collection enhancement very closely matches that seen for the pump wavelength (not shown). The electric fields above the planar Au surface drop to a very low value due to the destructive interference between the incident and reflected waves. Given the finite conductivity of Au, light penetrates into the metal up to skin depth and hence results in a finite field magnitude at the surface. On randomly roughened surfaces it is those fields that drive plasmonic resonances to give rise to notable, but uncontrollable SERS signal enhancements. For a metasurface with a groove depth of 70 nm, the absolute square of the electric fields at the entrance of the groove is notably enhanced

for the pump and Raman-shifted wavelength (Figure 5c), as roughly a quarter of a gap SPP wavelength fits along the depth of the grooves. This explains the notable NRE for that groove depth. Finally, for the groove depth of 178 nm the absolute square of the electric fields falls below the absolute square of electric field values for the planar Au surface. As a result, we observe a suppression of the NRE by ~40%.

In conclusion, we have demonstrated that metasurfaces can serve as a tunable SERS substrate that offers a robust enhancement of Raman signals of 25−50 times as compared to smooth metallic films. The creation of an anisotropic metasurface led to a factor 2 difference in the signal enhancements for the G and 2D, bringing to light the tensorial nature of the Raman polarizability for graphene. The reduction of Raman background signal as compared to smooth metal substrates was also demonstrated. These findings point toward the possible use of patterned anisotropic metasurfaces to enhance and direct surface electric fields for studying the symmetry properties of phonon modes supported by 2D layers and ultrathin films. Moreover, these 2D material-coated metasurface SERS substrates could provide a favorable platform for probing the orientation and symmetry of bond vibrations of molecules that can be deposited on top of the 2D materials.

METHODS

The metasurfaces are prepared by depositing an optically thick (~275 nm) metallic (Au) film on a 300 nm silica layer over a Si wafer using electron beam evaporation. We mill groove arrays of varying widths and depths into the Au layer using a FEI Helios FIB tool. Three sets of metasurfaces are designed, where within each set the groove widths are kept constant, but the depths are varied from 30 to 210 nm. The first set (set A) corresponds to 75 nm wide grooves, the second (set B) to 95 nm wide grooves, and the third (set C) to 170 nm wide grooves. Commercially available CVD graphene (from ACS Material) is then transferred onto the fabricated metasurfaces. We illuminate the graphene-based metasurfaces with a green laser at a wavelength of 532 nm and record the Raman spectra of graphene using a confocal optical microscope connected to a spectrometer (Witec Alpha 500). In order to perform near-normal incidence on our sample, we employ a 20×, 0.4 NA objective in the path of the incident green laser. All metasurfaces were patterned into a single substrate, and this afforded a straightforward quantitative comparison of the Raman spectra.

AUTHOR INFORMATION

Corresponding Author
*E-mail: brongersma@stanford.edu.

ORCID
Mark L. Brongersma: 0000-0003-1777-8970

Notes
The authors declare no competing financial interest.

REFERENCES

(1) Raether, H. *Surface Plasmons on Smooth and Rough Surfaces and on Gratings*; Springer, 1988.

(2) Gramotnev, D. K.; Bozhevolnyi, S. I. Plasmonics beyond the diffraction limit. *Nat. Photonics* **2010**, *4*, 83−91.

(3) Albrecht, M. G.; Creighton, J. A. Anomalously intense Raman spectra of pyridine at a silver electrode. *J. Am. Chem. Soc.* **1977**, *99*, 5215−5217.

(4) Kneipp, K.; et al. Single molecule detection using surface-enhanced Raman scattering (SERS). *Phys. Rev. Lett.* **1997**, *78*, 1667−1670.

(5) Kerker, M.; Wang, D. S.; Chew, H. Surface enhanced Raman scattering (SERS) by molecules adsorbed at spherical particles: errata. *Appl. Opt.* **1980**, *19*, 4159−4174.

(6) Moskovits, M. Surface roughness and the enhanced intensity of Raman scattering by molecules adsorbed on metals. *J. Chem. Phys.* **1978**, *69*, 4159.

(7) Moskovits, M. Surface selection rules. *J. Chem. Phys.* **1982**, *77*, 4408−4416.

(8) Schatz, G. C., Young, M. A., Van Duyne, R. P. In *Surface-Enhanced Raman Scattering: Physics and Applications*; Kneipp, K., Moskovits, M., Kneipp, H., Eds.; Springer Berlin Heidelberg, 2006; pp 19−45, DOI: 10.1007/3-540-33567-6_2.

(9) Vo-Dinh, T.; Wang, H. N.; Scaffidi, J. Plasmonic nanoprobes for SERS biosensing and bioimaging. *J. Biophotonics* **2010**, *3*, 89−102.

(10) Sharma, B.; Frontiera, R. R.; Henry, A.-I.; Ringe, E.; Van Duyne, R. P. SERS: Materials, applications, and the future. *Mater. Today* **2012**, *15*, 16−25.

(11) Boybay, M. S.; Ramahi, O. M. Waveguide probes using single negative media. *IEEE Microw. Wirel. Components Lett.* **2009**, *19*, 641−643.

(12) Ramahi, O. M.; Ren, Z.; Boybay, M. S. Near-field probes using metamaterial inclusions for enhanced sensitivity. *Proc. IEEE Sensors* **2010**, 1681−1684.

(13) Gandra, N.; et al. Tunable and amplified Raman gold nanoprobes for effective tracking (TARGET): in vivo sensing and imaging. *Nanoscale* **2016**, *8*, 8486−8494.

(14) Astilean, S.; Bolboaca, M.; Maniu, D.; Iliescu, T. Ordered metallic nanostructures for surface-enhanced Raman spectroscopy. *Rom. Reports Phys.* **2004**, *56*, 346−351.

(15) Salisbury, W. W. Absorbent body for electromagnetic waves. U.S. Patent 2599944, 1943.

(16) Thareja, V.; et al. Electrically tunable coherent optical absorption in graphene with ion gel. *Nano Lett.* **2015**, *15*, 1570−1576.

(17) Schwanecke, A. S.; Fedotov, V. A.; Khardikov, V. V.; Prosvirnin, S. L.; Chen, Y.; Zheludev, N. I. Optical magnetic mirrors. *J. Opt. A* **2007**, *1*, 9−11.

(18) Esfandyarpour, M.; Garnett, E. C.; Cui, Y.; McGehee, M. D.; Brongersma, M. L. Metamaterial mirrors in optoelectronic devices. *Nat. Nanotechnol.* **2014**, *9*, 542−7.

(19) Mak, K. F.; Shan, J. Photonics and optoelectronics of 2D semiconductor transition metal dichalcogenides. *Nat. Photonics* **2016**, *10*, 216−226.

(20) Butler, S. Z.; et al. Progress, challenges, and opportunities in two-dimensional materials beyond graphene. *ACS Nano* **2013**, *7*, 2898−2926.

(21) Novoselov, K. S.; et al. Electric Field Effect in Atomically Thin Carbon Films. *Science (80-.).* **2011**, *306*, 666.

(22) Nair, R. R.; et al. Fine Structure Constant Defines. *Science (80-.).* **2008**, *320*, 2008.

(23) Vakil, A.; Engheta, N. Transformation Optics Using Graphene. *Science (Washington, DC, U. S.)* **2011**, *332*, 1291−1294.

(24) Zhang, Y.; et al. Direct observation of a widely tunable bandgap in bilayer graphene. *Nature* **2009**, *459*, 820−3.

(25) Ling, X.; et al. Can graphene be used as a substrate for Raman enhancement? *Nano Lett.* **2010**, *10*, 553−561.

(26) Ling, X.; et al. Raman Enhancement Eff ect on Two-Dimensional Layered Materials. *Nano Lett.* **2014**, *14*, 3033−3040.

(27) Schedin, F.; et al. Surface-enhanced Raman spectroscopy of graphene. *ACS Nano* **2010**, *4*, 5617−5626.

(28) Zhu, X.; et al. Enhanced light-matter interactions in graphene-covered gold nanovoid arrays. *Nano Lett.* **2013**, *13*, 4690−4696.

(29) Lee, J.; Shim, S.; Kim, B.; Shin, H. S. Surface-enhanced Raman scattering of single- and few-layer graphene by the deposition of gold nanoparticles. *Chem. - Eur. J.* **2011**, *17*, 2381−2387.

(30) He, S.; et al. Graphene-based high-efficiency surface-enhanced Raman scattering-active platform for sensitive and multiplex DNA detection. *Anal. Chem.* **2012**, *84*, 4622−4627.

(31) Khorasaninejad, M.; et al. Highly enhanced Raman scattering of graphene using plasmonic nano-structure. *Sci. Rep.* **2013**, *3*, 2936.

(32) Xu, W.; et al. Surface enhanced Raman spectroscopy on a flat graphene surface. *Proc. Natl. Acad. Sci. U. S. A.* **2012**, *109*, 9281−9286.

(33) Calizo, I.; Bao, W.; Miao, F.; Lau, C. N.; Balandin, A. A. The effect of substrates on the Raman spectrum of graphene: Graphene-on-sapphire and graphene-on-glass. *Appl. Phys. Lett.* **2007**, *91*, 1−4.

(34) Ferrari, A. C.; Basko, D. M. Raman spectroscopy as a versatile tool for studying the properties of graphene. *Nat. Nanotechnol.* **2013**, *8*, 235−46.

(35) Mooradian, A. Photoluminescence of metals. *Phys. Rev. Lett.* **1969**, *22*, 185−187.

(36) Lumdee, C.; Yun, B.; Kik, P. G. Gap-Plasmon Enhanced Gold Nanoparticle Photoluminescence. *ACS Photonics* **2014**, *1*, 1224−1230.

(37) Boyd, G. T.; Photoinduced Luminescence from the Noble Metals and its Enhancement on Roughened Surfaces. *Phys. Rev. B* **1986**, *33*, 7923.

(38) Pardo, F.; Bouchon, P.; Haidar, R.; Pelouard, J. L. Light funneling mechanism explained by magnetoelectric interference. *Phys. Rev. Lett.* **2011**, *107*, 1−4.

(39) Shin, J.; Shen, J. T.; Catrysse, P. B.; Fan, S. Cut-through metal slit array as an anisotropic metamaterial film. *IEEE J. Sel. Top. Quantum Electron.* **2006**, *12*, 1116−1121.

(40) Le Ru, E. C.; Etchegoin, P. G. Principles of Surface-Enhanced Raman Spectroscopy. *Princ. Surface-Enhanced Raman Spectrosc* **2009**, 1−27.

(41) Hanson, G. W. Dyadic Green's functions and guided surface waves for a surface conductivity model of graphene. *J. Appl. Phys.* **2008**, *103*, 064302.

(42) Falkovsky, L. A.; Pershoguba, S. S. Optical far-infrared properties of a graphene monolayer and multilayer. *Phys. Rev. B: Condens. Matter Mater. Phys.* **2007**, *76*, 153410 .

(43) Falkovsky, L. A.; Varlamov, A. A. Space-time dispersion of graphene conductivity. *Eur. Phys. J. B* **2007**, *56*, 281−284

(44) Falkovsky, L. A. Optical properties of graphene and IV ± VI semiconductors. *Phys.-Usp.* **2008**, *51*, 887−897 .

(45) Chandran, A.; Barnard, E. S.; White, J. S.; Brongersma, M. L. Metal-dielectric-metal surface plasmon-polariton resonators. *Phys. Rev. B - Condens. Matter Mater. Phys.* **2012**, *85*, 1−9.

(46) Yoon, D.; et al. Strong polarization dependence of double-resonant Raman intensities in graphene. *Nano Lett.* **2008**, *8*, 4270−4274.

(47) Li, Z.; et al. Quantitative determination of the spatial orientation of graphene by polarized Raman spectroscopy. *Carbon* **2015**, *88*, 215−224.